A Study of The Active Galactic Nucleus of NGC 4593 with Adaptive Optics Assisted Data from the Integral Field Spectrograph MUSE

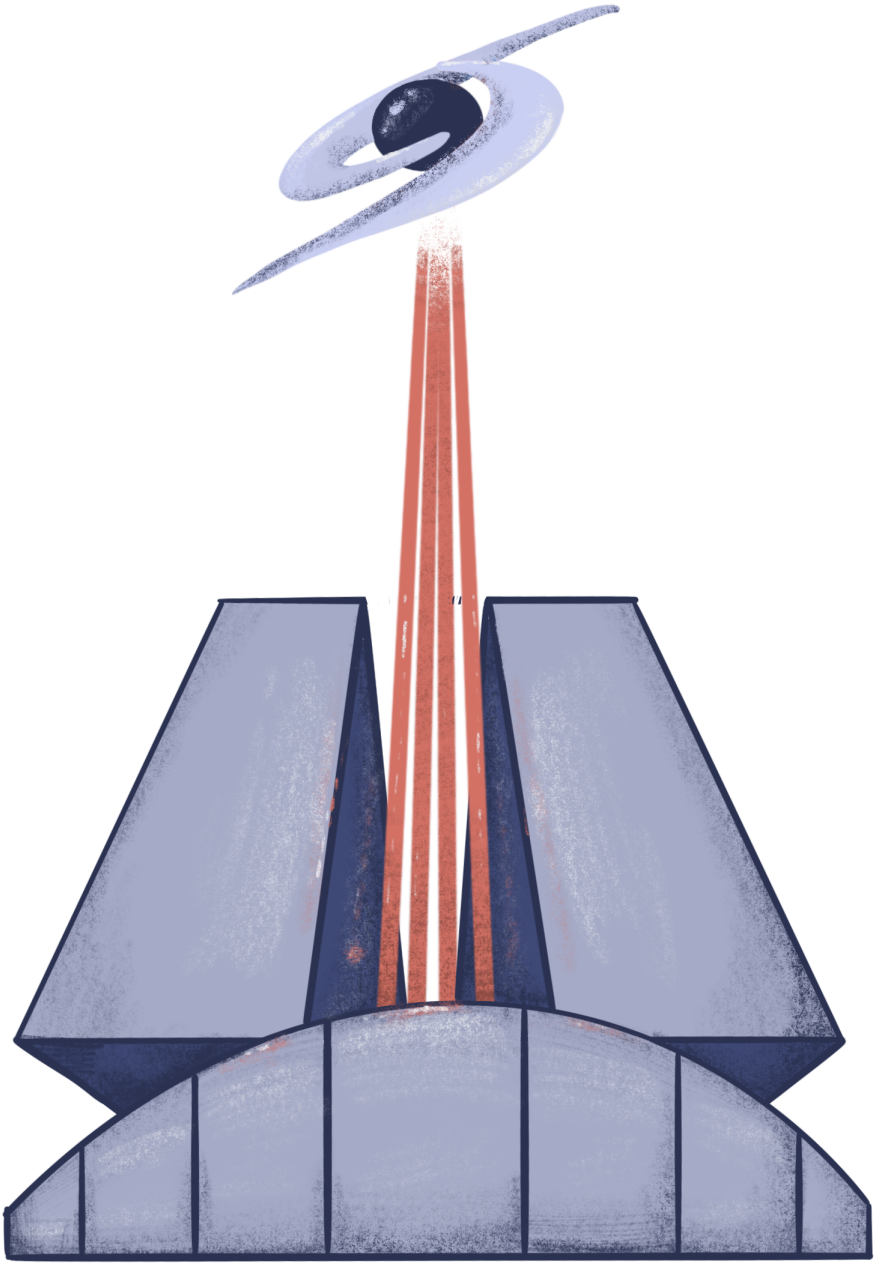

Illustration by Celia Fernández Martín

TRABAJO DE FIN DE GRADO
Universidad de La Laguna
Facultad de Física
Julio 2021

Autora: **Paula Sosa Guillén**
Tutor: **Sébastien Comerón**

Contents

1 Resumen

Los Núcleos Activos Galácticos son fenómenos altamente energéticos que se producen en la región central de algunas galaxias masivas. Consisten en la acreción de materia hacia un agujero negro súper masivo situado en la región central. Este fenómeno es crucial para entender la morfología y evolución de las galaxias. Existen muchos tipos de galaxias que tienen esta característica. En concreto nos interesan las tipo Seyfert 1 que se reconocen debido a la fuerte emisión en lineas espectrales anchas.

En el trabajo que nos ocupa se estudia la región central de la galaxia NGC 4593, una galaxia de tipo Seyfert 1. El cubo de datos usado para su estudio se toma con el espectrógrafo de campo integral MUSE (instalado en el Very Large Telescope). Este instrumento permite acceder a una calidad muy buena en la observación astronómica, en parte proporcionada por las cuatro estrellas de guía láser que permiten corregir la turbulencia atmosférica, y a su gran campo de visión. NGC 4593 es una galaxia tipo espiral caracterizada por tener dos anillos: uno interno (anillo nuclear) y otro mayor en la zona mas externa de la galaxia. Además, muestra lineas de emisión muy anchas en las lineas Hβ, Hγ y Fe II.

La metodología usada para llevar a cabo el análisis se basa en el uso del software `GIST`, que nos ha permitido realizar el tesselado Voronoi a partir de los píxeles recogidos en un cubo de datos que ha pasado un pre-procesado. Una vez se hace el tesselado Voronoi es posible proceder con el estudio de la cinemática estelar con el programa pPXF. A partir del cual se obtiene el comportamiento de las estrellas y se obtienen los mapas de velocidades. Para lograr un buen ajuste de los espectros se han enmascarado las lineas de emisión de la zona central y las longitudes de onda asociadas al láser utilizado por el telescopio. Así, se han podido obtener unos buenos resultados de la cinemática.

Con los datos recogidos por este estudio se ha estudiado la cinemática y la morfología de la región central de la galaxia comprendida en el campo de visión ($4\farcs5 \times 4\farcs5$). Se han expuesto los mapas de velocidades y se han tratado debidamente. Además, se ha estudiado la imagen de la galaxia, obtenida a partir del cubo de datos, con el software DS9 permitiéndonos hacer un estudio del brillo superficial. En última instancia se ha hecho, con un código de python, un graficado de la curva de rotación de la región interna de NGC 4593.

Finalmente, se han extraído conclusiones con respecto a los resultados obtenidos durante el trabajo. En estos, se recogen los aspectos más relevantes tanto de las técnicas de análisis de datos como de la morfología que presenta NGC 4593.

De esta forma el trabajo está estructurado en diferentes bloques en base a lo anteriormente comentado: una introducción para situarnos en el contexto teórico de lo que se trata, los objetivos que se abordan en el trabajo, la metodología aplicada para la obtención de resultados (la línea de trabajo que se ha seguido y los programas usados), los resultados junto con la discusión de estos y, por último, la conclusión del trabajo.

2 Introduction

Abstract

En esta sección se presenta el contexto, desde un punto de vista teórico, de los aspectos que se estudian en el trabajo. En primer lugar, se introduce el concepto de núcleo activo galáctico así como se enumeran y explican algunos de los diferentes tipos que se conocen. Además, se enfatizan las galaxias tipo Seyfert, que es el grupo al que pertenece la galaxia en cuestión de estudio: NGC 4593. Adicionalmente, se explican conceptos de la cinemática estelar, enfatizando en conceptos como el sigma-drop. A continuación, se presenta MUSE, un instrumento de última generación de alta resolución integrado en el Very Large Telescope, en Chile, y a partir del cual se han obtenido los datos de estudio. Además, se hace un repaso de las características de la galaxia NGC 4593 que se conocen hasta la fecha. Por último, esta sección cuenta con un apartado dedicado a las curvas de rotación en galaxias espirales, puesto que en el estudio que hacemos se trabajará con este concepto.

2.1 Active Galactic Nuclei

Active galactic nuclei (AGN hereafter) are often found at the centre of massive spiral, elliptical, and S0 galaxies. AGN are intense energetic phenomena which occur in the innermost part of a galaxy. The brightness of AGN is very high and it is not associated with any radiation emanating from star formation. It comprehends a luminosity ranging from 10^{42} to 10^{48} erg s^{-1} [Troncoso, 2009].

AGN are a manifestation of the accretion of matter into a Super Massive Black Hole (SMBH hereafter). Due to the angular momentum of the infalling material, this process occurs through inwards spiralling within an accretion disk. This accretion is a fundamental part of our knowledge of galaxies since it affects the host galaxy through feedback, allowing us to understand their evolution and the different phenomenologies that they present. As science has progressed, close links have been established between AGN, the host galaxy and the central SMBH. For example, a tight relation can be seen between the BH mass and the velocity dispersion of the ionised gas [Ferrarese and Merritt, 2000].

2.1.1 AGN types

According to their luminosities and spectral properties, the AGN can be subdivided into different types, some of them are: Quasars, Radio galaxies, LINERs, Blazars, and Seyfert Galaxies.

Quasars. Also known as Quasi-Stellar Objects, they are the brightest AGN type. Their luminosity is usually about a thousand times greater than that of their entire host galaxy. Therefore, it is often difficult to detect the underlying galaxy, and we can only see their nucleus emission, hence, we merely have a few host galaxies well defined, those that are close enough to be observed [Ramos Almeida, 2009]. Whereas quasars themselves are easy to detect due to the high luminosity emitted. Different studies have shown that quasars were more active in the past. For instance, Schmidt et al. [1995] date the peak of the quasar activity around 2.5×10^9 years after the Big Bang. Also, some studies have revealed that the gas around AGN is metal-rich, reinforc-

ing the concept of quasar formation early in the history of the universe.

Radio Galaxies. These galaxies are very luminous at radio wavelengths. This is due to synchrotron processes [1] that occurs at the galactic centre [Burbidge, 1956]. Radio wavelengths can be detected at large distances, and hence, these galaxies are a useful tool in cosmology. The most intense radio galaxies are large elliptical galaxies, and they can be sub-dived into two different types depending on their optical spectrum: the broad-line radio galaxies and the narrow-line radio galaxies.

LINERs. The Low-ionisation Nuclear Emission-line Region are the lowest luminosity type of AGNs. They are characterised by an optical spectrum chiefly dominated by emission lines from low ionisation atoms, as well as by deep absorption of stellar bands [Heckman, 1980]. LINERs are the main AGN type found in spiral galaxies.

Blazars are AGN similar to Seyfert or quasars galaxies. However, they are characterised by the line of sight to the central engine: Blazars have the jet (located at the centre of the galaxy) pointing towards the observer [Urry and Padovani, 1995]. Through this, they mask the absorption and emission of the optical spectral lines. Blazars are highly variable radio and gamma-ray sources, with quick fluctuations with periods of days or hours.

In this paper, I am studying NGC 4593, a Seyfert 1 galaxy. **Seyfert Galaxies** are well known because of their intense emission in spectral lines. Also, they have a bright nucleus that can be observed in a huge spectral range (from radio to X-rays). In 1943, Carl Seyfert established a categorisation for the brightness of the central regions of galaxies, making it possible the classification of the Seyfert Galaxies in several sub-types.

2.1.2 Unified Model of Seyfert Galaxies

There are two types of Seyfert galaxies: Seyfert 1 and 2 (Sy 1 and Sy 2, hereafter). In the Sy 1 case, the spectrum is characterised by broad emission lines (as for example in Hβ, Hγ, and Hα [Osterbrock, 1977]) and a deep continuum stellar emission, while Sy 2 galaxies do not show broad lines, having instead a low intensity continuum [Ramos Almeida, 2009], as we can see in Figure 1. The broad and the narrow lines are generated in different regions of the innermost galactic disc. The narrow lines are produced by low-density ionised gas: the Narrow Line Region (NLR hereafter), and the broad lines are produced by high-density optically thick ionised gas: the Broad Line Region (BLR hereafter). The BLR is much closer to the centre of AGN than the NLR [Ramos et al., 2009].

After many studies, a Unified Model has been established [Antonucci, 1993]. The model posits that the difference between Sy 1 and Sy 2 AGN is an orientation effect, being both different views of the same object as we can see in Figure 2.

[1] Synchrotron radiation: It is electromagnetic radiation produced by charged particles that are accelerated.

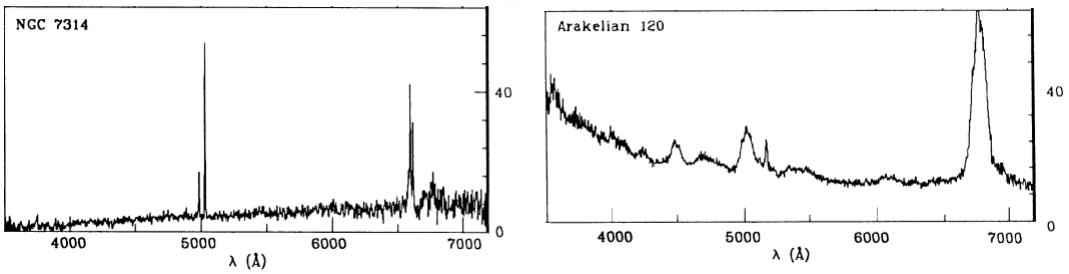

Figure 1: Spectra of the two chief types of Seyfert galaxies. *Left Panel*: A Seyfert 2 galaxy, NGC 7314. *Right panel*: A Seyfert 1 galaxy, Arakelian 120. Notice how the emission lines for the Sy 1 are wider than that for Sy 2. Figure taken from Winkler [1992].

Sy 1s have a direct line of sight fixed to the nucleus, allowing us to see the innermost parts of the galaxy, where the broad lines are generated, whereas Sy 2s present an obscuration of these lines due to dust, distributed in a doughnut-shaped torus [Ricci et al., 2011]. Further subdivisions of Sy galaxies exist, depending on the orientation of the AGN: these result in different optical spectra. These objects have been classified as type 1.2, 1.5, 1.6, 1.7, or 1.8.

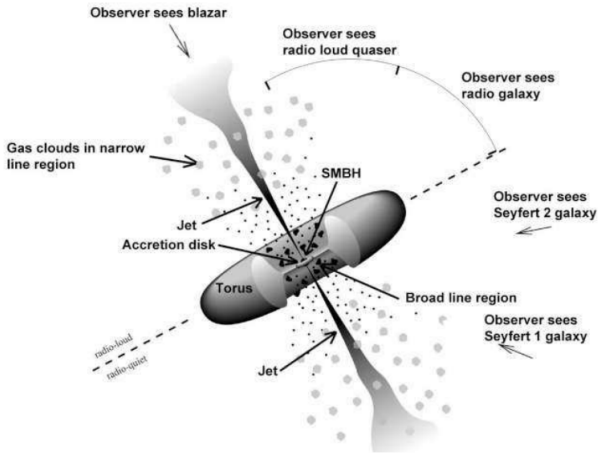

Figure 2: Schematic view of the Unified Model of AGN. On the right side, we can observe the line of sight differences between Sy 1 and Sy 2 galaxies. Taken from Tello [2014].

2.2 Stellar Kinematics in spiral galaxies

We are going to study two different concepts related to the Line Of Sight Velocity Distribution (LOSVD hereafter), which are the **velocity** and the **velocity dispersion**.

On one hand, the velocity, $V_\star$, is understood as the average velocity of the stars in each bin. The galaxy has a relative motion away from us (as observers), due to the expansion of the universe and the rotational movement of the object. Each bin has a slightly different velocity from the global motion of the galaxy.

On the other hand, we work with the velocity dispersion, $\sigma_\star$. Each bin has an average speed, however, the stars included in a specific bin do not have the same velocity as they can move away from this average. Therefore, the velocity dispersion describes the standard deviation of the velocity of the stars in that bin. This has direct consequences on the galaxy's morphology. If we have a low $\sigma_\star$ compared with the circular velocity of rotation, the galaxy will have a disc, whereas, if $\sigma_\star$ is high, the galaxies do have a large random motion and do not present a clear disc morphology [Girardi et al., 1993].

2.2.1 Sigma-Drop, σ-drop

The σ-drop phenomenon is known as a dip in the velocity dispersion. It seems intuitive that the velocity dispersion increases in the central region of a galaxy due to the presence of a slowly-rotating bulge and a SMBH. However, often a low-velocity dispersion region is found at the centre of spiral galaxies.

In Comerón et al. [2008] and in Wozniak et al. [2003] they suggest that σ-drop phenomenon are caused by a recent star formation process.

Stars are born into a circumnuclear rotating disk of cool gas. The gas and dust are stoked, increasing the density until they collapse and star formation begins.

The gas clouds cannot get velocity in the vertical direction due to the viscosity: they are continuously colliding. However, the stars are point sources that do not collide with each other, hence, they can reach a considerable vertical velocity (due to gravitational effects that generate a "kinematical heating"), making their σ to increase.

Star formation begins from flat disks and with time the disk gains thickness, passing from less than a hundred parsecs in thickness, at the beginning, to kiloparsecs at old ages. That happens because the newly-born stars have inherited the kinematics of a dinamically cold gas disc.

A σ-drop due to star formation is a long-lived phenomenon. When the star formation falls, the velocity dispersion takes time, from hundreds of Myr to Gyr [Comerón et al., 2008], to increase.

Often we relate σ-drops with nuclear rings because they usually host huge star formation regions.

2.3 MUSE data

To observe and obtain information about many different astronomical objects, the European Southern Observatory (ESO) has developed The Multi-Unit Spectroscopic Explorer (MUSE), an instrument integrated into the Very Large Telescope (VLT) in the Atacama Desert, in northern Chile (see Figure 3). The data of NGC 4593 used in this paper were obtained with MUSE.

Figure 3: The Cerro Paranal hosting the Unit Telescopes of the Very Large Telescope. Figure taken from the *ESO Images*.

MUSE is an integral field spectrograph operating in the visible and near-infrared wavelength range (**4750 Å - 9300 Å**), with a wide Field Of View (FOV hereafter) compared to others integral field spectrographs. Also, it is equipped with an adaptive optics (AO hereafter) system known as GALACSI that can provide a significant performance boost on the MUSE angular resolution [Bacon et al., 2010]. This system uses four sodium Laser Guide-Stars (Na-LGS) sent from one of the Telescope Units of the VLT. The light emitted by these lasers is then collected by four Wave Front Sensors (WFS) which are connected to a Real-Time Computer, SPARTA,

which estimates the distortion introduced by the Earth's atmosphere, and calculates the correction that must be applied to obtain sharp data [Stuik et al., 2006].

MUSE splits the FOV into 24 sub-fields, each one fed into a spectrograph, called Integral Field Unit (IFU hereafter), producing a spatially resolved spectrum. MUSE has two different modes. On one hand, it has the Wide Field Mode (WFM) with a FOV of $1' \times 1'$ and, on the other hand, the Narrow Field Mode (NFM) with a FOV of $7\farcs5 \times 7\farcs5$, being the one that uses the Na-LGS AO [Bacon et al., 2010]. Thanks to the NFM of MUSE, we can analyse the centre of NGC 4593 in detail.

2.4 NGC 4593

NGC 4593 is an AGN galaxy that is also known as MRK 1330 or MCG -01-32-032. Its position is right ascension RA = $12^{h}39^{m}39^{s}$, and declination $\delta = -0.5°20'39\farcs34$ [2].

This galaxy is classified as (R)SB(rs)b by De Vaucouleurs et al. [2013] and Buta et al. [2015]. It has a flattened disk with a pronounced bar (of 10.3 kpc in length [Comerón et al., 2010]) and a two-armed spiral structure with a central galactic bulge. This bulge is important in NGC 4593 because it host a bright compact nucleus [Davies et al., 2015]. Additionally, it has many tightly wound spiral arms with two rings: one innermost faint ring (a nuclear ring) and an enormous outer ring around the outskirts of the galaxy (of 3.54 arcmin in projected major axis diameter [Comerón et al., 2014]) as we can see in Figure 4. Furthermore, the strong bar, present in this galaxy, drives gas inwards, affecting the motion of stars and their distribution [Kim et al., 2020].

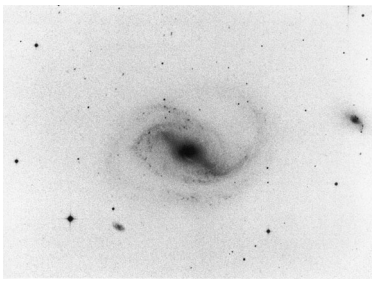

Figure 4: Image optical taken at the *du Pont* telescope of NGC 4593.

As we can extract from Comerón et al. [2010], the nuclear ring presented by the galaxy is a star-forming nuclear ring that has a relative size of 0.070 (ring diameter divided by D_o, defined in Bottinelli et al. [1995] as the angular diameter size of the galactic disc), with a semimajor axis of 880 pc.

This galaxy has been ambiguous concerning the activity type as it is close to the boundary between a Seyfert 1 and a Seyfert 1.2 [Davies et al., 2015], due to the strong broad Hβ component presented comparing to a Sy 1 galaxy [Osterbrock, 1977]. Nevertheless, we will consider NGC 4593 as a Sy 1 [Marín et al., 2007]. It shows bright broad emission lines in Hβ, Hγ, and Fe II [Cackett et al., 2018].

NGC 4593 has a redshift of $z = 0.00900$ [Torricelli-Ciamponi et al., 2014], with a distance of $D = 35.35 \pm 0.50$ Mpc [Makarov et al., 2014]. The diameter of NGC 4593 is of 39.25 kpc [Davies et al., 2015]. Also, it has a central BH that has been studied by different scientists, mainly in the X-ray range. They concluded that the logarithm of the BH mass, in solar mass units is $M_{BH} = 7.0$ [Torricelli-Ciamponi et al., 2014].

[2] `https://ned.ipac.caltech.edu/`

2.5 Rotation curves in spiral galaxies

The rotational curve of a spiral galaxy is the rotational velocity of the observable material (stars, gas, and dust) as a function of the radial distance from the galaxy's centre. This representation has been used by astronomers as a method to calculate the mass of the galaxy. If we consider a spherical model for the galaxy, we obtain the relation [Lequeux, 1983]:

$$V^2 = \frac{GM(R)}{R} \tag{1}$$

Where V is the rotational velocity of the observable material, G the constant of the gravitation, M is the mass inside a spheric radius, and R is the radius of the galaxy from the centre.

Hence, the theoretical behaviour of the rotational curve will present a Keplerian fall outside the radius where the disc starts to fade out, with $V \sim 1/R^{1/2}$. However, many studies such as Begeman et al. [1991], Sofue and Rubin [2001] or Salucci and Frenk [1989] show that rotation curves do not decay. As we can see in Figure 5 the curve does not fall, it remains constant at a certain value of V as R increases. While R grows, V is constant at $\sim 200 - 300\,\mathrm{Km\,s^{-1}}$ in large spiral galaxies [Burbidge, 1975].

The flat behaviour in the rotational curves has been explained as a mass effect. The most extended theory support that spiral galaxies are surrounded by a massive halo of dark matter, in which $M(R) \propto R$.

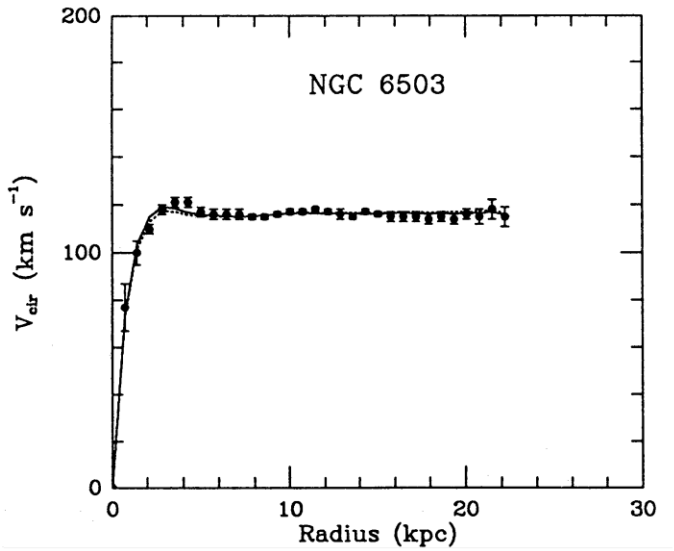

Figure 5: Rotational curve of NGC 6503 taken from Begeman et al. [1991].

3 Objectives

Abstract

El objetivo principal de este Trabajo de Fin de Grado es el de conocer y utilizar diferentes herramientas técnicas que se utilizan profesionalmente en la espectroscopia de campo integral actual. Se utiliza el paquete de tratamiento de datos `GIST`, incluyendo las técnicas de tesleado Voronoi, la obtención de mapas de velocidades de las estrellas con pPXF y el uso del software DS9. He trabajado desde el sistema operativo Linux, familiarizándome con este y aprendiendo a usar la línea de comandos integrada.

Para lograr este objetivo se ha estudiado el centro de la galaxia NGC 4593, en el cual se encuentra un núcleo activo galáctico de tipo Syfert 1. A partir de los datos recolectados con el instrumento MUSE, se ha podido llevar a cabo esta tarea.

Este trabajo incluye también el objetivo de la ampliación del conocimiento teórico sobre los núcleos activos galácticos. Además de permitirme acercarme, desde un punto de vista instrumental y observacional, al mundo de la astronomía.

The main objective of this work is to **learn and use different tools used in integral field spectroscopy**. We have used the data processing package `GIST`, which includes the Voronoi Tesselation method and the obtention of stellar velocity maps with pPXF. Also, I started to learn to use the DS9 software. To reach this objective, I had to use the operative system Linux, where I have download all the software required to develop the work. Through the analysis of the central region of NGC 4593, we could use all the technical tools specified above. This has trained me to process data cubes and I could apply the knowledge acquired with NGC 4593 to other galaxies.

This galaxy, being a Seyfert 1, hosts an active galactic nucleus. Hence, this work also has the objective of extending my theoretical knowledge on the field of active galaxies. All the data used have been taken by the MUSE instrument, therefore, I could work with real data and make a consistent data processing.

I also have the objective of studying specific characteristics from NGC 4593, through reading previous studies and with my results. We analysed different aspects from in the central region of the galaxy and worked with concepts as the superficial brightness and the rotational velocity.

Another objective of this work was to apply different concepts of astronomy, such as the technical terminology and the distance units used in the field of galactic studies.

My thesis has a format, in some aspects, similar to a scientific article. Therefore, as an objective, I have improved the use of LaTeX, the technical English, and above all, I have read papers and learnt physics through them.

From an academic point of view, my objective was the application of physics in a research environment. I have seen how the workplace could be and learned from people such as my tutor, that is integrated into the research community. I have learned about the interpretation of scientific data, the communication of prob-

lems, ideas, and solutions.

As a personal objective, I could know if I really feel comfortable with this field of study. I used this opportunity to choose a possible way to dedicate myself professionally in the future.

4 Methodology and Data Processing

Abstract

Para el estudio y tratamiento de datos de NGC 4593 se han tenido en cuenta varios aspectos que son contemplados en esta sección. En primer lugar se citan y explican algunas de las estrategias de observación que se deben tener en cuenta a la hora de recoger datos con un telescopio (bias, corriente oscura, flat field, etc). A continuación, se recoge brevemente cómo ha sido la obtención de datos, considerando el tiempo de exposición y la secuencia de cielo-objeto durante la observación. También se explica, a grandes rasgos, la estructura de la fase de pre-procesamiento que siguen los datos del instrumento MUSE. Se enfatiza en el `GIST` pipeline software que se ha usado en el tratamiento de datos, considerando los aspectos que se han utilizado: el análisis de la cinemática estelar y el Teselado Voronoi. A este último se le ha dedicado una sección en la que se explica qué es y en qué consiste el método de teselado. Adicionalmente, se indica cómo y con qué condiciones se estudia la cinemática estelar. Por último, se hace una breve mención al software de astronomía DS9 que se utiliza durante el análisis de datos.

To study and analyse the central region of NGC 4593 we use a data cube obtained from the ESO archive. It offers science-ready data known as 'Phase 3' data. These data have been pre-processed by ESO through the MUSE pipeline. Each telescope pointing, returns a 3D final data cube (with two spatial and one spectral coordinate) and another one containing the error.

4.1 Observation Strategies

During the pre-processing phase the astronomical data are calibrated to obtain a data cube with science-ready quality. The different steps that take place in the pipeline are aimed at, among others things, taking the following factors into account.

- Bias: To avoid pixels with zero or negative count values that could be problematic for the data processing, the CCD is preset to a roughly constant base number of counts. The bias frames are also able to correct the read-out noise of the CCD.

  To make this possible, we have to take some images with zero exposition time and with the shutter closed. Then, we obtain the average/ median/ resistant mean bias.

$$\mathrm{BIAS} = \overline{\mathrm{bias}} \tag{2}$$

  BIAS ≡ Master bias. $\overline{\mathrm{bias}}$ ≡ Average/ median/ resistant mean of individual bias frames.

- Dark current: The temperature induces a thermal noise in the CCD that turns into a signal: the dark current. To eliminate this effect it is necessary to take images (with the shutter closed) with an exposure time comparable to the science data exposures.

$$\mathrm{DARK} = \overline{\left(\frac{\mathrm{darks} - \mathrm{BIAS}}{t_{\mathrm{darks}}}\right)} \tag{3}$$

  DARK ≡ Master dark. darks ≡ Individual darks frames. t_{darks} ≡ Dark time exposure.

- Flat field: As a result of the geometrical distribution of the CCD panels, not all the pixels have the same sensitivity. This happens, among other reasons, because of the dimensional differences of the optical path. Each pixel can return a different value from the same luminosity source, presenting different sensitivities.

  To correct this, the telescope has to point during the twilight to a place where there are no bright stars, and take some frames of a few seconds to characterise the flat field.

$$\text{FLAT} = \overline{\text{N}(\text{flat} - \text{BIAS} - \text{DARK} \cdot t_{\text{flat}})} \quad (4)$$

FLAT ≡ Master flat. flat ≡ Individual flat frames. t_{flat} ≡ Flat time exposure. N ≡ Normalisation constant.

Considering these three aspects, it is possible to have a final image, corrected from the above presented instrumental effects:

$$\text{IMAGE} = \overline{\left(\frac{\text{image} - \text{BIAS} - \text{DARK} \cdot t_{\text{image}}}{\text{FLAT}}\right)} \quad (5)$$

IMAGE ≡ Combined data. image ≡ Individual data frames. t_{image} ≡ Image time exposure.

At this point, the flux calibration has to be considered. Due to some factors, such as the state of the atmosphere or the quality of the telescope, the data obtained can have many lost photons, affecting the estimated luminosities. So, the idea is to take images of a known star and compare the observed luminosity with the real luminosity. With this process we can extract a multiplicative factor that gives an account on the atmospheric absorption.

Working on a data cube (that is the case of the topic in this paper) which has a spectral dimension, it is recommendable to also calibrate that aspect. Each pixel has a specific wavelength. So, the camera has to point to a calibration lamp that shows a set of known spectral lines to analyse the wavelength corresponding to each pixel. This depends a lot on the temperature, that is why the calibration has to be done just before (or just after) as the observations.

During the observation of a galaxy the sky has an emission. Sometimes, and especially in infrared, the sky can be brighter than the object observed. To solve this problem, the astronomers have to take images from the sky away from the target and subtract its contribution to the object image. Due to the quick changes in the sky, it becomes necessary to make sequences of observation of the sky and the object during the data collection.

4.2 Data obtention

The data obtained to study the central region of NGC 4593 were taken during the night of April 20, 2019 with Jahnke Knud as principal investigator. With the MUSE-NFM AO, $8 \times 600\,\text{s}$ on-target exposures intertwined with $2 \times 200\,\text{s}$ off-target exposure of the sky were collected. The sequence was: object - object - sky - object - object - object - object - sky - object - object. Fortunately, all exposures were taken with enough angular resolution and quality to be used.

The raw data were pre-processed with the MUSE pipeline and also have experienced Voronoi Binning. Now, because more than a

year has passed since the data acquisition, we can freely access the data in the ESO archive.

4.3 Pre-Processing Phase

The data reduction follows different steps, done by the ESO MUSE data reduction pipeline. First, the raw files are pre-processed with the recipe `muse_scibasic`, able to convert the pixels of the CCD into a table (dividing geometrically the field of view and adjusting the wavelength associated with each pixel). This recipe also takes into account the bias and the flat-fielding.

Second, the blank sky observations, taken during the data obtention, are also processed with the recipe `muse_create_sky` to generate two different files: the sky line emission and the sky continuum spectrum.

Next, the object files are processed again, now, using the sky information with the recipe `muse_scipost`, capable of subtracting the sky contamination and correcting the exposure from the atmospheric refraction. Finally the data are resampled into a data cube.

At this point, we obtain for each data cube, two files: IMAGE_FOV (a 2D image of the FOV, obtained by collapsing the data cube along its spectral axis) and a PIXEL_TABLE (which contains the information required to build the data cube but stores the coordinates of each pixel in a table). Then, the IMAGE_FOV files, for each pointing, are processed with `muse_exp_align`. This recipe estimates the shift that are required to align the data cubes.

Finally, the PIXEL_TABLE files are processed too with `muse_exp_combine`, which is in charge of applying the alignment correction and resampling the data cubes. Therefore, the result of MUSE pipeline process gives back the combined data cube and a combined IMAGE_FOV. At this point, we have all information ready for scientific analysis [Weilbacher et al., 2020].

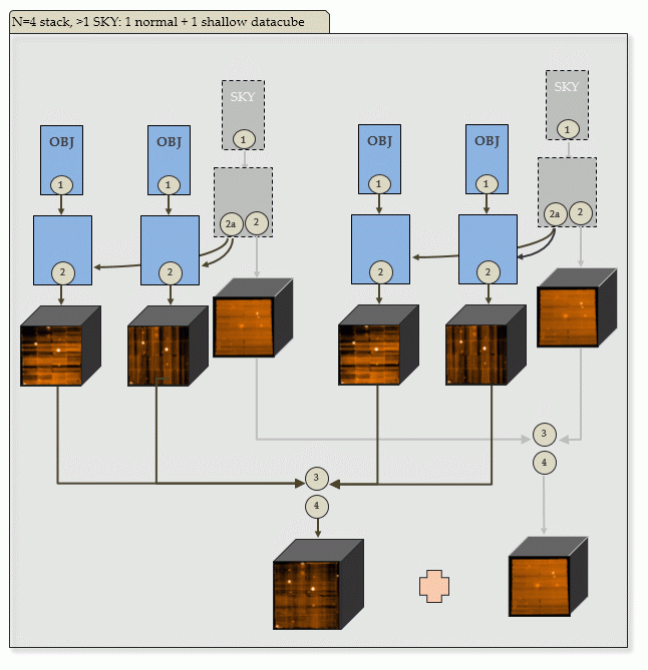

Figure 6: Illustration of the Data Cube Analysis taken from the *ESO* Phase 3 *Data Release Description*.

To sum up, if our data set has [N] object exposures and [M] sky exposures, the output will be one combined data cube of the object observed and another one, also combined, from the sky files, plus two IMAGE_FOVs corresponding to each data cube. The data cubes have two extensions, one with the signal and other with the estimated uncertainties. In the Figure 6 we can see a visual representation of the process.

The data obtained from the ESO archive that I have used to make this study has already passed this pre-processing phase.

4.4 The GIST pipeline

The pre-processed data cube has been processed through the Galaxy IFU Spectroscopy

Tool (GIST), an all-in-one software able to conduct a complex analysis of data cubes [Bittner et al., 2019]. GIST is entirely written in Python 3 and it let us extract the stellar kinematics, analyse the emission-lines, and show stellar population properties from the spectrum. This software is extremely useful and versatile due to the easily modifiable code architecture presented. Furthermore, GIST can work in many different settings, making it a perfect tool to use with MUSE.

The code is structured in three different parts: the **preparatory steps**; the **main analysis**, that extract information about many aspects; and the **visualization** [Bittner et al., 2019].

We are interested in two main aspects:

- **Voronoi Binning** of the cube, where we can choose the Signal-to-Noise ratio of the spectra with which we want to work with. This is implemented during the preparatory step.
- The **stellar Kinematics analysis**: GIST uses the pPXF routine, that is widely explained in Cappellari and Emsellem [2004]. pPXF allows us to have a stellar spectrum fitted with a lineal combination of stellar templates with different ages and chemical compositions which are shifted and broadened to take into account the kinematics on the line of sight velocity distribution.

This software includes a visualization routine called Mapviewer, which is a sophisticated graphical user interface. It has been made specifically to show all data processed by this pipeline, where we can see all the properties (as the spectrum, kinematics fits or stellar population fits) of each Voronoi bin by simply clicking on it in a map of the FOV.

4.5 Voronoi Binning

Voronoi Binning is a processing data technique able to produce an adaptative spatial binning to obtain bins with a desired Signal-to-Noise ratio (S/N hereafter), providing the maximum possible angular resolution in 2D. As we have already seen, when the data have passed through Phase 3, we obtain a data cube with two extensions. One with the signal, and the other one with the estimated uncertainty.

It is possible to calculate the S/N ratio in a bin formed by n pixels:

$$\frac{S}{N} = \frac{\sum_{i=1}^{n} S_i}{\sqrt{\sum_{i=1}^{n} \sigma_i^2}} \tag{6}$$

Where S_i is the signal associated to each pixel i and σ_i corresponds to the uncertainty.

To work with astronomical objects it is often necessary to locally average the data together to do a good scientific analysis. The Voronoi Binning technique, named as Voronoi Tesselation (VT hereafter), allows us to have a roughly constant S/N value in each bin. Indeed, bigger bins will appear in the low S/N regions and the smaller ones will be in the high S/N regions (giving more resolution).

We work with the code written by Cappellari and Copin [2003] within GIST to produce a Voronoi Binning. The technique has to satisfy some aspects: The bins generated by the code have not overlapping spaxels or holes in the final data. The shape of the bins has to be compact (as round as possible). And, the number of bins presented in our data has to be as small as possible, but without sacrificing the spatial resolution. These three aspects are known as **topological**, **morphological**, and **uniformity** requirement respectively.

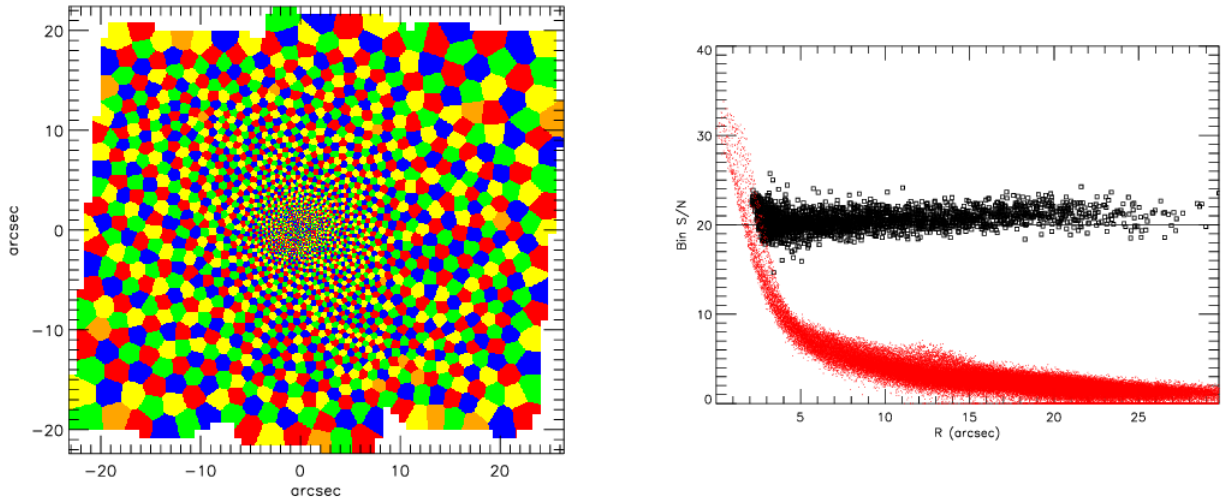

Figure 7: Example of Voronoi Binning. Figure from Cappellari [2009]. *Left Panel*: CVT binning method from an image with 350000 pixels, gathered into 3000 bins. *Right panel*: S/N Scatter from the CVT method above. In red S/N of the original pixels, in black the $(S/N)_{bin}$ of each bin. The target is $(S/N)_T = 20$.

To satisfy all requirements, the VT applies the called Centroidal Voronoi Tessellation (CVT hereafter) method, which can generate a tailored distribution of pixels into bins. Through some computational developments based on the Lloyd method (1982), Cappellari and Copin could create a system able to bin the scientific data to be then analysed, as we can see in Figure 7.

Spatial Binning is crucial for the study of stellar kinematics, the topic in this paper. All the bins in the extraction of kinematics require to have a similar S/N, so the properties estimated for each of them are comparable.

We have binned the data with a signal-to-noise ratio of 25 in the wavelength range $5400 - 5600$Å.

4.6 Stellar kinematics processing

Through `GIST`, using pPXF, we can fit the velocity $V_\star$ and the velocity dispersion $\sigma_\star$ (explained in Section 2.2). We have also used MILES, that is a library of stellar populations spectra with different metallicities and ages, called stellar population templates [Falcón-Barroso et al., 2011]. In the spectral range of interest, MILES has a spectral resolution of 2.51Å in FWHM [Beifiori et al., 2011].

In our study of the kinematics, we work with a wavelength range of **4800 Å - 6690 Å**. We could not work with a wider spectrum because my laptop did not have enough RAM. We have not considered the regions redder than 7000Å due to the presence of prominent sky lines, bringing noise to the final data.

Some spectral emission lines have to be masked for running pPXF. The wavelength range associated with the AO corrections, which include 5780Å to 6050Å, is affected by the laser guide of the AO. Also, some galaxy emission lines with prominent peaks have been masked with a width of 30Å, and we have additionally masked the contribution of the Hβ line with a mask 120Å in width and the [N II] with a mask 180Å in width. The masked lines are shown in Table 1.

Line	Wavelength [Å]	Width [Å]
Hβ	4861.32	120
[O III]	4958.83	30
[O III]	5002.77	30
[N I]	5200.39	30
[O I]	6300.20	30
[O I]	6363.67	30
[N II]	6547.96	180
Hα	6562.80	30
[N II]	6583.34	30

Table 1: Emission lines masked for the analysis of stellar kinematics.

4.7 DS9 Software

SAOImage DS9 is an astronomical data visualisation software. It allows to work, perform, edit or make regions and colormaps manipulation with FITS images and binary tables.

We have used this software to further analyse our NGC 4593 data. We have learned to change the thresholds and contrast, activate different luminosity scales, measure sizes of elements on the image, and produce surface brightness contours.

5 Results

Abstract

En esta sección se presentan los resultados obtenidos durante el tratamiento de datos que se ha realizado. En primer lugar, se hace un estudio del mapa de velocidades obtenido a partir del procesado de datos con `GIST` y la herramienta de visualización gráfica `Mapviewer`. Se exponen tanto el mapa de velocidades como el de la dispersión de velocidades, así como los mapas asociados a los errores de ambos parámetros. Se hace una relación entre dichos resultados y la morfología de la galaxia NGC 4593. A continuación, se trata el mapa de luminosidad con el software DS9, esbozando las isofotas y comentando las características mas relevantes. Por último, se ha hecho un tratamiento de datos a través del lenguaje de programación python para obtener las dos curvas de rotación (aquella asociada a las velocidades positivas y otra para las negativas) de la galaxia analizada.

5.1 NGC 4593 Morphology

In this section, we try to find correlations between the behaviour of LOSVD maps, and the morphology of the host galaxy.

We present in Figure 8 the stellar kinematics maps obtained during the `GIST` pipeline processing of the NGC 4593 MUSE data cube.

We work with a radius of 4 arcsec in data, as we can observe in the axis of the maps. This angular FOV allows us to see a small portion of the central region of NGC 4593, $\sim 700\,\mathrm{pc}$ in side.

5.1.1 *Galactic Bulge*

The most striking feature is the structure of $V_\star$ map. We can detect a rapidly rotating disc. If we observe the velocity dispersion behaviour, we see a relatively high σ structure ($\sim 100\,\mathrm{km\,s^{-1}}$) enclosing the central region of the galaxy, that supports the idea of a galactic bulge located in the innermost region of the galaxy.

The galactic bulge is understood as a small stellar spheroid formation inside a galactic disc. We found a $\sigma_\star \sim 100\,\mathrm{km\,s^{-1}}$, that is comparable with what Valenti et al. [2018] found for The Milky Way: a velocity dispersion of $\sigma = 119\,\mathrm{km\,s^{-1}}$, which is much larger than the typical σ for the disc [Lewis and Freeman, 1989]. Hence, we conclude that we have a large $\sigma_\star$ bulge in the innermost region of NGC 4593.

5.1.2 *Nuclear ring*

As we could read in Section 2.4, the nuclear ring presented in NGC 4593 has 880 pc in radius, which implies a 5.2 arcsec semimajor axis, and as we can observe, our data includes less than 4 arcsec. We are, then, inside of the nuclear ring, making it impossible to see.

If NGC 4593 has a σ-drop related to the nuclear ring we could not see it in our data, because the drop in σ would fall outside of the FOV.

5.1.3 *Strong Bar*

Apart from what we have seen in maps, it is important to take into account the presence of a bar in NGC 4593.

The galaxy presents a prominent bar (Section 2.4), that drives matter to the central region. That can make us think about the possi-

ble role that the bar could have in the velocity dispersion map. However, in the study of 20 different galaxies made by Comerón et al. [2008], it has been established that the presence of a bar does not affect directly behaviour of the σ at the centre of galaxies.

We could not study the properties of the bar of NGC 4593 because it has a 10.3 kpc in length and we work with a FOV of barely 700 pc in side.

5.1.4 Treatment of errors

The errors in the LOSVD maps during the pPXF routine process are illustrated in Figure 9. The typical error for the velocity is about $12\,\mathrm{km\,s^{-1}}$, except at the centre, where the error increase being lager than $30\,\mathrm{km\,s^{-1}}$. The velocity dispersion error is slightly higher, in general, at around $20\,\mathrm{km\,s^{-1}}$, and in the central region it exceeds $40\,\mathrm{km\,s^{-1}}$.

This is important to analyse the data obtention. We can disregard the central information due to the big error presented.

Also, on the right-down side of the $\sigma_\star$ map, we observe a weak increase on the dispersion level, we relate this with a bad fit due to some noise in the signal.

5.1.5 pPXF fits

The big uncertainty found at the centre is due to the broad emission lines of the AGN that make it hard to study the underlying stellar continuum. In fact, we can see this in Figure 10. We show the pPXF fit in two different bins of the data: one is from a central bin, as we have already said, the fit is bad and we cannot obtain a good LOSVD fit; the second one is a bin further away from the centre, presenting a good fit.

In Figure 11 we show the fit for the complete wavelength range studied. There we can see the difference in fits and how it changes between a central bin and an external one.

Therefore, we can observe two notable emission lines in the Hβ and Hα lines as we expect from a Seyfert 1 galaxy, and also it presents a strong emission in [N II] line at 6547.96Å.

The velocity maps were made with the fit of Figure 10 and not with Figure 11, because the spectral range between 4800Å − 6690Å presents broad emission lines (such as Hβ and Hα) and the mask could not cover all the impact that they made, affecting the fits. That is why we use the 5050Å − 5700Å range for our final map. Unfortunately, these fits are still bad at the very centre of the galaxy. An examination of Figure 10 shows that this might be due to a line at 5303Å that we identify as [Fe XIV].

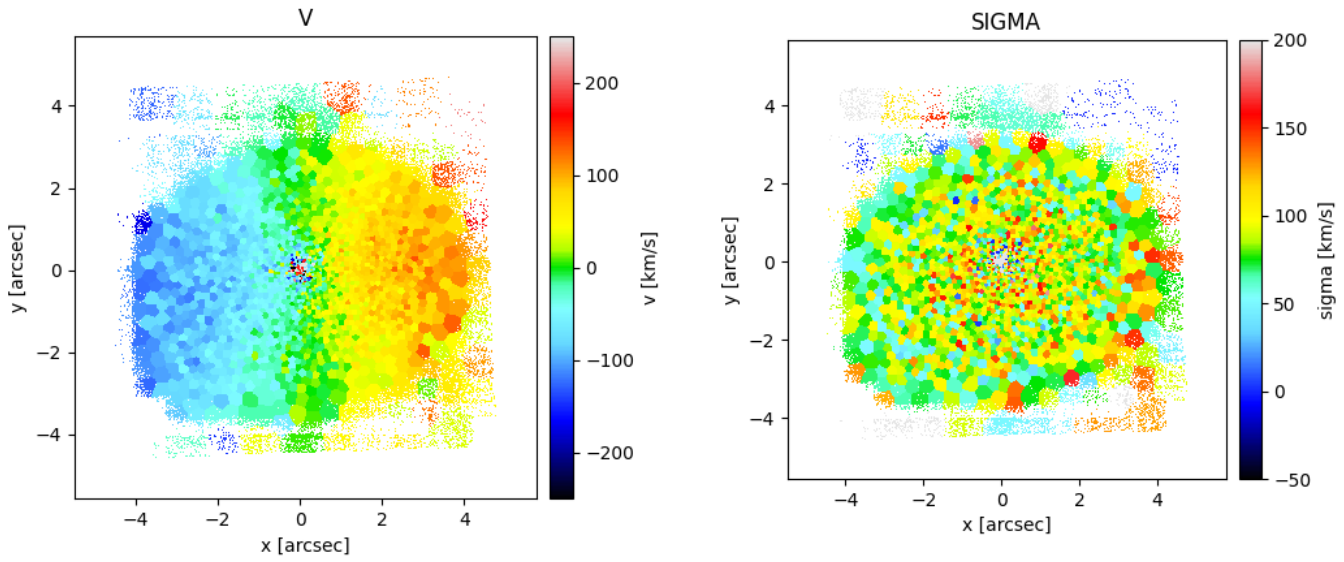

Figure 8: Kinematic momentum maps of NGC 4593. The colour scale is given at the right side of each graphic in units of $\mathrm{km\,s^{-1}}$. *Left panel:* Velocity distribution, $\mathrm{V}_\star$. *Right panel:* Velocity dispersion, $\sigma_\star$.

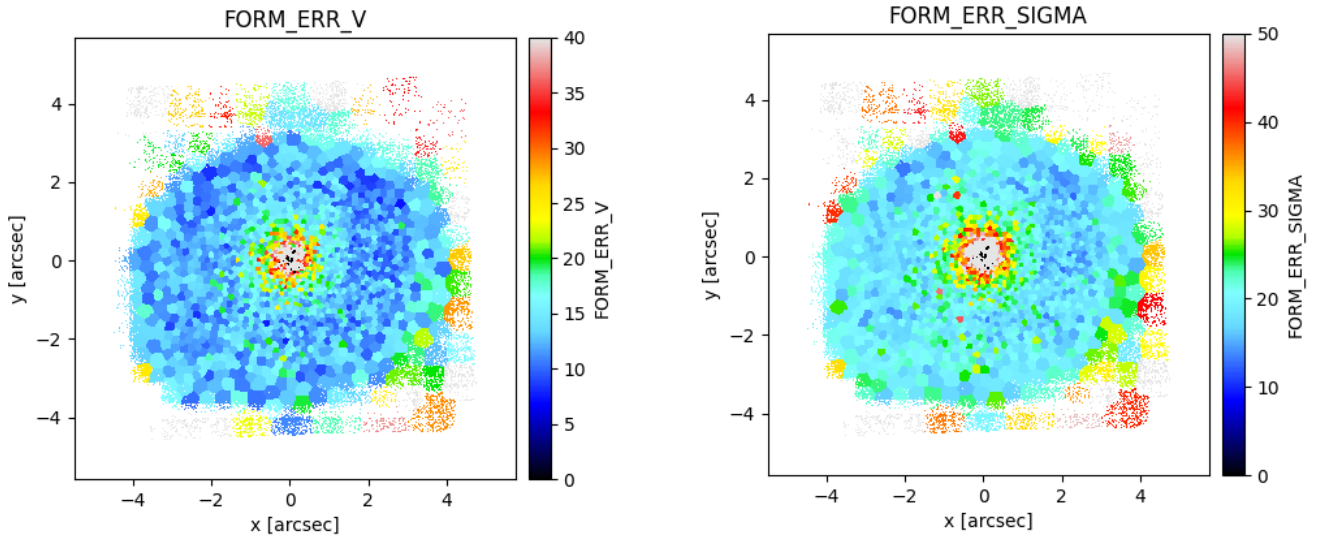

Figure 9: Kinematic momentum error maps of NGC 4593. The colour scale is given at the right side of each graphic in units of $\mathrm{km\,s^{-1}}$. *Left panel:* Velocity distribution error, $\Delta\mathrm{V}_\star$. *Right panel:* Velocity dispersion error, $\Delta\sigma_\star$.

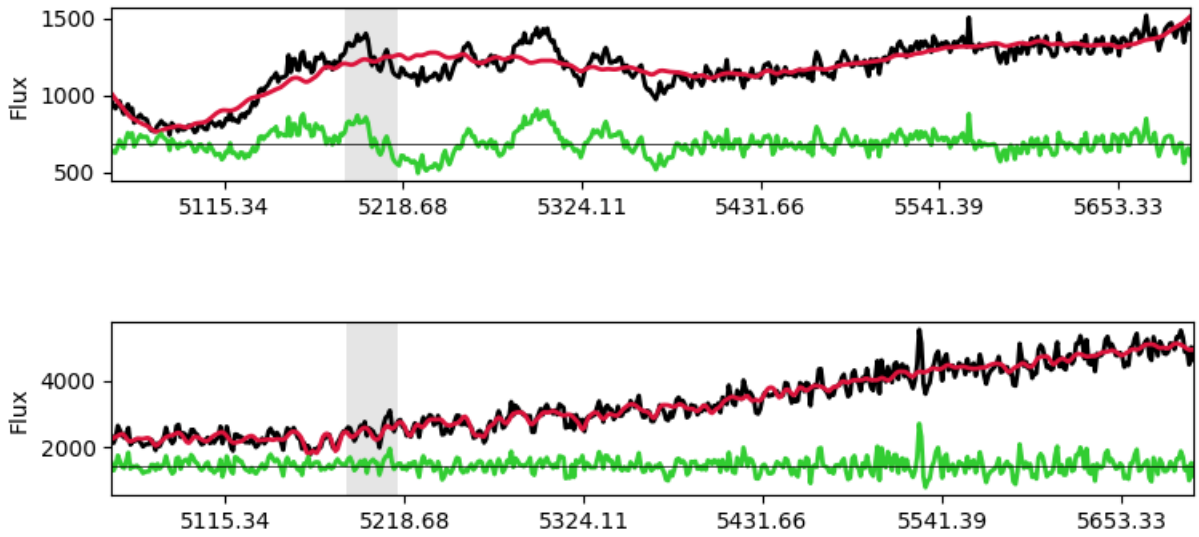

Figure 10: MUSE spectra of two different bins in the central region of NGC 4593. Here we show the pPXF fits made in the wavelength range of 5050Å − 5700Å, the range without prominent emission lines. The flux for each bin has units of $10^{-20}\,\mathrm{erg\,cm^{-2}\,\AA^{-1}\,s^{-1}}$. *Top panel:* Fit of a galaxy's region strongly affected by the AGN emission. *Bottom panel:* Fit of a galaxy's region less affected by the AGN emission.

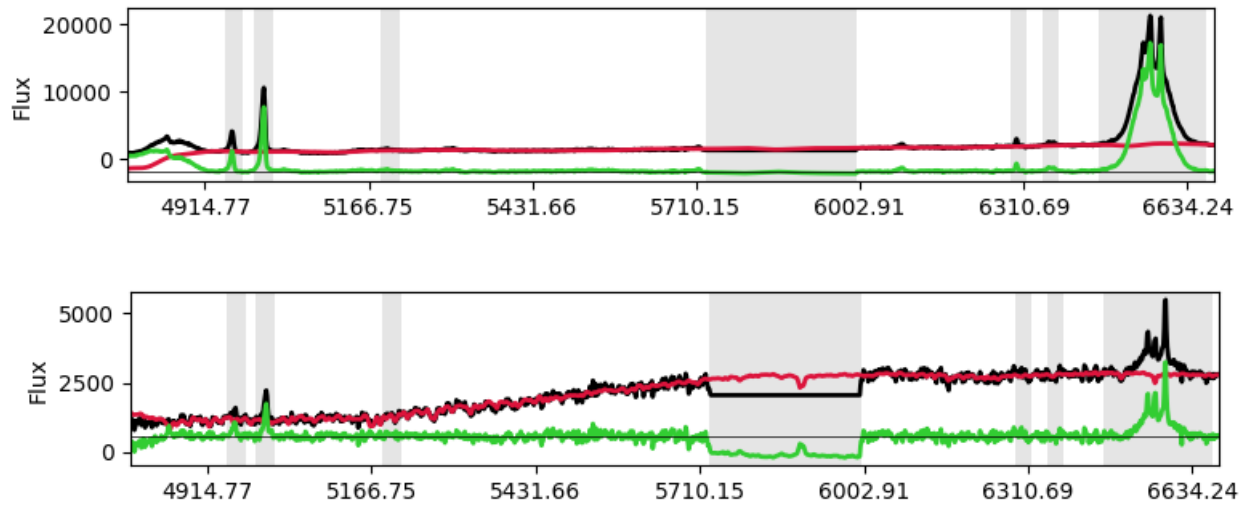

Figure 11: MUSE spectra of two different bins in the central region of NGC 4593. Here we show the pPXF fits made in the wavelength range of 4800Å − 6690Å, the whole range with prominent emission lines masked. The flux for each bin has units of $10^{-20}\,\mathrm{erg\,cm^{-2}\,\AA^{-1}\,s^{-1}}$. Notice that the line emission Hβ (at 4861.32Å) seems to not to be masked but that is due to a visualisation problem of the `Mapviewer` software and actually this line is masked for the fit. *Top panel:* Fit of a galaxy's region strongly affected by the AGN emission. *Bottom panel:* Fit of a galaxy's region less affected by the AGN emission.

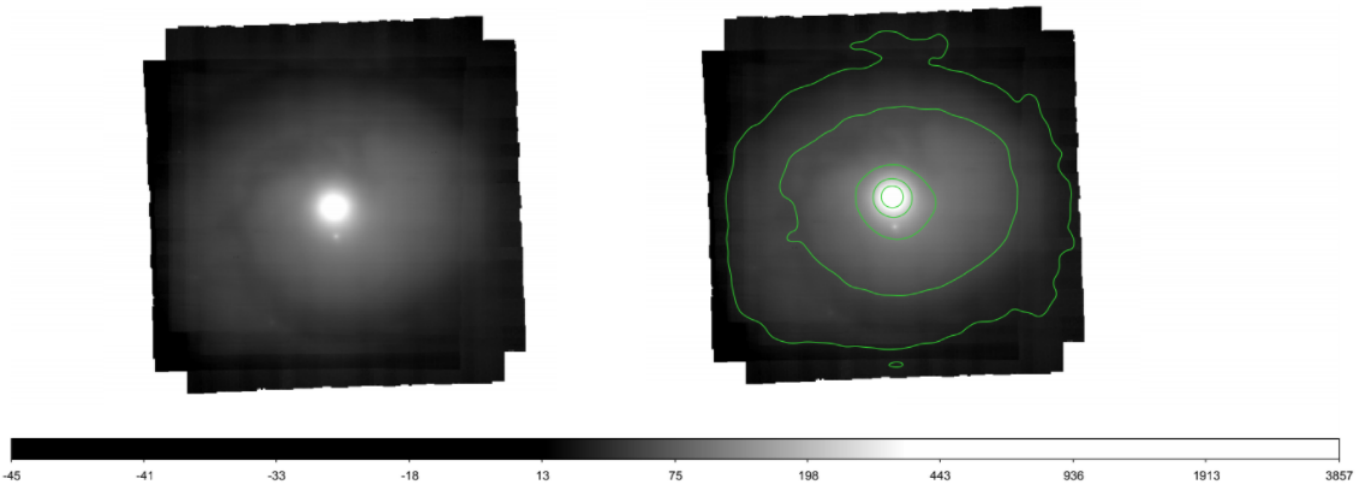

Figure 12: *Left panel:* Surface brightness map as seen with DS9 obtained by collapsing the MUSE data along the spectral axis (IMAGE_FOV), with a black and white color scale (at the bottom) in units of $10^{-20}\,\mathrm{erg\,cm^{-2}\,\AA^{-1}\,s^{-1}}$ *Right panel:* Same as the left map, but including the isophotes in green lines.

5.2 NGC 4593 surface brightness

We have studied the luminosity map obtained by the MUSE pipeline by collapsing the data cube along its spectral axis (IMAGE_FOV data produced) with the DS9 tool. In Figure 12 we can clearly see the surface brightness map.

In the left map, we can observe a low surface brightness spiral region probably due to a speck of dust and gas converging on the nucleus. Probably, at a small scale, this might contribute at feeding the AGN.

In the right map, we have obtained the isophotes curves logarithmically spaced in intensity (at 500, 250, 125, 62.5 and 31.25 10^{-20} $\mathrm{erg\,cm^{-2}\,\AA^{-1}\,s^{-1}}$). They are characterised by a rather smooth and elliptical morphology, indicating the lack of strong star formation clumps.

The isophotes are situated in the innermost region of the galaxy within the nuclear ring. In the outer part of the map, the isophotes represent those regions dominated by star, whereas, the internal ones are associated with the bright nuclear region dominated by the AGN emission.

5.3 Rotation curves of NGC 4593

In the data analysis of NGC 4593, we have made a velocity curve of the central region.

First, we have to find the major axis to make the velocity profile. Going to the HYPERLEDA database, we have found that the position angle of the major axis is PA = 46.6°. However, looking at the rotational velocity map obtained in our analysis, we can determine that the kinematic major axis has to be associated to $y \sim 0$ arcsec, with a PA = 90°. We know it because we can see that the innermost region has the line of zero velocity at $x \sim 0$.

Hence, we conclude that the major axis of NGC 4593 changes with radius. This coincides with the orientation of the isophotes seen in Figure 12.

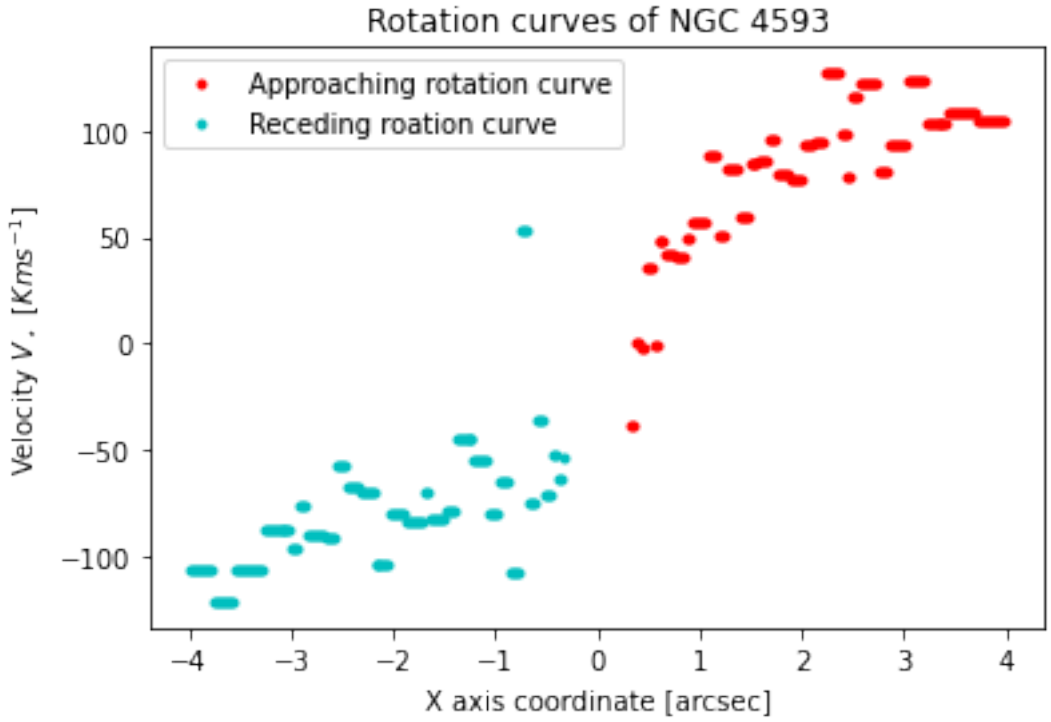

Figure 13: Rotation curves of NGC 4593 without the correction in the inclination angle. We represent the x-axis versus the velocity $V_\star$. In soft blue the positive rotation, in hard blue the negative rotation.

To plot the rotational curve, we take $y = \pm 0.0125$ arcsec, and all the values for x and $V_\star$ associated with these y. Now, we make a plot of the approaching rotation curve (with positive values of x-axis) and the receding rotation curve (with negative values of x-axis). We can see in Figure 13 both curves.

Comparing with the Figure 5 of the galaxy NGC 6503 seen in Section 2.5, we can observe that the tendency is the same. However, in the central region of NGC 4593, inside the radius where the rotation has been measured, the velocity does not became exactly constant, likely that is because we work with a maximum radius of 700 pc. Probably this innermost region has more errors because we are near to the central BH, where we have more non-circular and random motion than in the outer regions.

Moreover, it can be possible that the velocity still increase with radius outside the FOV before becoming constant.

5.3.1 NGC 4593 central region mass

Our study allows us to know how much mass there is inside 4 arcsec in NGC 4593. Using the equation 1 we can obtain this value.

We have to take into account that the real circular velocity of the galaxy is $V\,(\sin i)^{-1}$, where i is the inclination angle between the line of sight and the polar axis of NGC 4593, listed in HYPERLEDA as $i = 34°$.

Hence, the mass is given by:

$$M(R) = \frac{R\left(\frac{V}{\sin i}\right)^2}{G} \tag{7}$$

We use $R = 700\,\mathrm{pc}$, $V = 120\,\mathrm{km\,s^{-1}}$ and $G = 6.674 \cdot 10^{-11}\,\mathrm{N\,m^2\,kg^{-2}}$. Finally, we obtain that within 4 arcsec we have a total mass of:

$$M(R \sim 4\,\mathrm{arcsec}) \sim 7 \times 10^9 M_\odot \tag{8}$$

6 Conclusions

Abstract

En esta sección se exponen las conclusiones del trabajo, que cumplen con los objetivos citados en la Sección 3.

Se concluye que el aprendizaje de las diferentes herramientas de análisis de datos astronómicos se ha realizado satisfactoriamente. Se ha aprendido a trabajar con archivos FITS, con el software `GIST`, con `Mapviewer` y con el software DS9.

Se enumeran las conclusiones del análisis espectroscópico de NGC 4593 hecho a través de MUSE. Hemos observado las siguientes características: Un bulbo galáctico en la región más interna (con $\sigma \sim 100\,\mathrm{km\,s^{-1}}$), fuerte presencia de las lineas Hβ y Hα, una espiral de polvo y gas convergiendo hacia el núcleo galáctico y un cambio en la posición del semi eje mayor de la galaxia según estamos en las regiones más internas o en las externas. Además, la curva de rotación de NGC 4593 muestra una tendencia típica presente en las regiones centrales de las galaxias espirales, pudiendose calcular la masa de galaxia contenida en los 4 arcsec internos, obteniendo una masa de $\sim 7 \times 10^9 M_\odot$.

6.1 Technical features conclusions

From a technical point of view, it is concluded that the learning of the different astronomical data analysis tools has been successfully completed.

i. I have learned how to work with FITS files with several programs.

ii. I have acquired knowledge about how to use the `GIST` software for data processing by modifying the study parameters (wavelength ranges, masking of emission lines, S/N ratio ...) from the MasterCongif and SpecMask_KIN files. These are the ones that have allowed me to carry out many tests before getting the final kinematics maps of NGC 4593.

iii. I have learned to work with the graphical visualisation tool `Mapviewer`, being able to extract maps and interpret them. We have also worked with fits and other parameters such as the modification of the scale or the graphics displayed by `Mapviewer` (not only kinematics maps could be represented, but we can also access other graphics that show different aspects, such as the surface brightness, or the S/N in each Voronoi Bin).

iv. I have learned to use the astronomical visualisation software DS9. I have been able to analyse surface brightness maps. We have worked concepts such as threshold change, luminosity scales (in our case we focused on logarithmic scales due to the large dynamical range in brightness), the measurement of lengths within the image, or the generation of surface brightness contours.

6.2 NGC 4593 features conclusions

On the other hand, the spectroscopic analysis of NGC 4593, done with MUSE, gave us the means to make the first approach to this galaxy's characteristics. We have studied its stellar kine-

matic properties, the surface brightness, and the velocity curves. Thus, from the MUSE results we have been able to reach the following conclusions:

i. NGC 4593 presents a central region with a $\sigma_\star \sim 100\,\mathrm{km\,s^{-1}}$, which most likely correspond to a bulge.

ii. It has been previously studied that NGC 4593 has a nuclear ring and a strong barred structure. However, through our study these morphologies could not be observed due to the small FOV of MUSE (we talk about 700 pc versus 900 pc and 10.3 kpc), witch is smaller than these two structures.

iii. It has also been found that the central spectra show strong emission in the Hβ and Hα emission lines, as expected for a Seyfert 1 galaxy. These, as well as other emission lines already mentioned in this paper, have been masked to obtain a good fit of the stellar kinematics.

iv. NGC 4593 has a spiral lane of dust and gas converging towards the galactic nucleus. This infalling material is characterised by a lower surface brightness than the surroundings. Other than that, the central region of NGC 4593 has smooth and elliptical isophotes.

v. If we observe the outskirts region of NGC 4593, we can see that the semi-major axis has an angular position of PA = 46.6° (according to HYPERLEDA), while if we observe the innermost 700 pc in the central region, we can conclude, derived from the kinematic study, that the semi-major is close to PA = 90°.

vi. The rotational curve of the innermost region of NGC 4593 presents a trend similar to that other spiral galaxies. However, due to the proximity to the nucleus, it is likely that we are not observing the region of the galaxy where a constant rotational velocity is achieved.

vii. We have obtained the mass contained within the central 4 arcsec of the galaxy. We concluded that $M(R \sim 4\,\mathrm{arcsec}) \sim 7 \times 10^9 M_\odot$

References

Israel Matute Troncoso. *Evolución de Núcleos Activos de Galaxias en el Infrarrojo*. PhD thesis, Universidad de La Laguna, 2009.

Laura Ferrarese and David Merritt. A fundamental relation between supermassive black holes and their host galaxies. *The Astrophysical Journal Letters*, 539(1):L9, 2000.

Cristina Ramos Almeida. *Actividad nuclear y formación estelar en galaxias*. PhD thesis, Universidad de La Laguna, 2009.

Maarten Schmidt, Donald P Schneider, and James E Gunn. Spectrscopic ccd surveys for quasars at large redshift. iv. evolution of the luminosity function from quasars detected by their lyman-alpha emission. *The Astronomical Journal*, 110:68, 1995.

Geoffrey R Burbidge. On synchrotron radiation from messier 87. *The Astrophysical Journal*, 124:416, 1956.

TM Heckman. An optical and radio survey of the nuclei of bright galaxies-activity in normal galactic nuclei. *Astronomy and Astrophysics*, 87:152–164, 1980.

C Megan Urry and Paolo Padovani. Unified schemes for radio-loud active galactic nuclei. *Publications of the Astronomical Society of the Pacific*, 107(715):803, 1995.

DE Osterbrock. Spectrophotometry of seyfert 1 galaxies. *The Astrophysical Journal*, 215:733–745, 1977.

C Almeida Ramos, Nancy A Levenson, JM Rodríguez Espinosa, Almudena Alonso-Herrero, A Asensio Ramos, James T Radomski, Chris Packham, R Scott Fisher, and Charles M Telesco. The infrared nuclear emission of seyfert galaxies on parsec scales: Testing the clumpy torus models. *The Astrophysical Journal*, 702(2):1127, 2009.

Robert Antonucci. Unified models for active galactic nuclei and quasars. *Annual review of astronomy and astrophysics*, 31:473–521, 1993.

H Winkler. Variability studies of seyfert galaxies–ii. spectroscopy. *Monthly Notices of the Royal Astronomical Society*, 257(4):677–688, 1992.

Claudio Ricci, Roland Walter, TJ-L Courvoisier, and Stephane Paltani. Reflection in seyfert galaxies and the unified model of agn. *Astronomy & Astrophysics*, 532:A102, 2011.

Jorge Dıaz Tello. *INVESTIGANDO EL FIN DE FORMACION ESTELAR EN GALAXIAS MASIVAS*. PhD thesis, Universidad Nacional de Córdoba, 2014.

Marisa Girardi, A Biviano, G Giuricin, Fabio Mardirossian, and Marino Mezzetti. Velocity dispersions in galaxy clusters. *The Astrophysical Journal*, 404:38–50, 1993.

S Comerón, JH Knapen, and JE Beckman. On the morphology of sigma-drop galaxies. *Astronomy & Astrophysics*, 485(3):695–705, 2008.

H Wozniak, F Combes, E Emsellem, and D Friedli. Numerical simulations of central stellar velocity dispersion drops in disc galaxies. *Astronomy & Astrophysics*, 409(2):469–477, 2003.

R Bacon, M Accardo, L Adjali, H Anwand, S Bauer, I Biswas, J Blaizot, D Boudon,

S Brau-Nogue, J Brinchmann, et al. The muse second-generation vlt instrument. In *Ground-based and Airborne Instrumentation for Astronomy III*, volume 7735, page 773508. International Society for Optics and Photonics, 2010.

Remko Stuik, Roland Bacon, Ralf Conzelmann, Bernard Delabre, Enrico Fedrigo, Norbert Hubin, Miska Le Louarn, and Stefan Ströbele. Galacsi–the ground layer adaptive optics system for muse. *New Astronomy Reviews*, 49 (10-12):618–624, 2006.

Gérard De Vaucouleurs, Antoinette de Vaucouleurs, G Harold Jr, Ronald J Buta, Georges Paturel, Pascal Fouqué, et al. *Third Reference Catalogue of Bright Galaxies: Volume III*, volume 3. Springer Science & Business Media, 2013.

Ronald J Buta, Kartik Sheth, E Athanassoula, Albert Bosma, Johan H Knapen, Eija Laurikainen, Heikki Salo, Debra Elmegreen, Luis C Ho, Dennis Zaritsky, et al. A classical morphological analysis of galaxies in the spitzer survey of stellar structure in galaxies (s4g). *The Astrophysical Journal Supplement Series*, 217(2):32, 2015.

Sébastien Comerón, JH Knapen, JE Beckman, E Laurikainen, H Salo, I Martínez-Valpuesta, and RJ Buta. Ainur: Atlas of images of nuclear rings. *Monthly Notices of the Royal Astronomical Society*, 402(4):2462–2490, 2010.

Richard I Davies, Leonard Burtscher, David Rosario, Thaisa Storchi-Bergmann, Alessandra Contursi, Reinhard Genzel, Javier Gracia-Carpio, E Hicks, Annemieke Janssen, Michael Koss, et al. Insights on the dusty torus and neutral torus from optical and x-ray obscuration in a complete volume limited hard x-ray agn sample. *The Astrophysical Journal*, 806 (1):127, 2015.

S Comerón et al., H Salo, E Laurikainen, JH Knapen, RJ Buta, M Herrera-Endoqui, J Laine, Benne W Holwerda, K Sheth, MW Regan, et al. Arrakis: atlas of resonance rings as known in the s4g. *Astronomy & Astrophysics*, 562:A121, 2014.

Minbae Kim, Yun-Young Choi, and Sungsoo S Kim. Effect of bars on evolution of sdss spiral galaxies. *Monthly Notices of the Royal Astronomical Society*, 494(4):5839–5850, 2020.

L Bottinelli, L Gouguenheim, G Paturel, and P Teerikorpi. Extragalactic database. vi. inclination corrections for spiral galaxies and disk opaqueness in the b-band. *Astronomy and Astrophysics*, 296:64, 1995.

VÍctor M Muñoz Marín, Rosa M González Delgado, Henrique R Schmitt, Roberto Cid Fernandes, Enrique Pérez, Thaisa Storchi-Bergmann, Tim Heckman, and Claus Leitherer. An atlas of the circumnuclear regions of 75 seyfert galaxies in the near-ultraviolet with the hubble space telescope advanced camera for surveys. *The Astronomical Journal*, 134(2):648, 2007.

Edward M Cackett, Chia-Ying Chiang, Ian McHardy, Rick Edelson, Michael R Goad, Keith Horne, and Kirk T Korista. Accretion disk reverberation with hubble space telescope observations of ngc 4593: evidence for diffuse continuum lags. *The Astrophysical Journal*, 857(1):53, 2018.

G Torricelli-Ciamponi, P Pietrini, G Risaliti, and M Salvati. Search for x-ray occultations in active galactic nuclei. *Monthly Notices of the Royal Astronomical Society*, 442(3):2116–2130, 2014.

D. Makarov, P. Prugniel, N. Terekhova, H. Courtois, and I. Vauglin. HyperLEDA. III. The catalogue of extragalactic distances. *A&A*, 570: A13, October 2014. doi: 10.1051/0004-6361/201423496.

J Lequeux. Rotation curves and masses of galaxies. *Astronomy and Astrophysics*, 125:394, 1983.

KG Begeman, AH Broeils, and RH Sanders. Extended rotation curves of spiral galaxies: Dark haloes and modified dynamics. *Monthly Notices of the Royal Astronomical Society*, 249 (3):523–537, 1991.

Yoshiaki Sofue and Vera Rubin. Rotation curves of spiral galaxies. *Annual Review of Astronomy and Astrophysics*, 39(1):137–174, 2001.

Paolo Salucci and Carlos S Frenk. The effect of the disc on the rotation curves of spiral galaxies. *Monthly Notices of the Royal Astronomical Society*, 237(1):247–256, 1989.

G Burbidge. On the masses and relative velocities of galaxies. *The Astrophysical Journal*, 196:L7–L10, 1975.

Peter M Weilbacher, Ralf Palsa, Ole Streicher, Roland Bacon, Tanya Urrutia, Lutz Wisotzki, Simon Conseil, Bernd Husemann, Aurélien Jarno, Andreas Kelz, et al. The data processing pipeline for the muse instrument. *arXiv preprint arXiv:2006.08638*, 2020.

Adrian Bittner, J Falcón-Barroso, B Nedelchev, A Dorta, DA Gadotti, M Sarzi, A Molaeinezhad, ENRICHETTA Iodice, D Rosado-Belza, A de Lorenzo-Cáceres, et al. The gist pipeline: A multi-purpose tool for the analysis and visualisation of (integral-field) spectroscopic data. *Astronomy & Astrophysics*, 628: A117, 2019.

Michele Cappellari and Eric Emsellem. Parametric recovery of line-of-sight velocity distributions from absorption-line spectra of galaxies via penalized likelihood. *Publications of the Astronomical Society of the Pacific*, 116(816): 138, 2004.

Michele Cappellari and Yannick Copin. Adaptive spatial binning of integral-field spectroscopic data using voronoi tessellations. *Monthly Notices of the Royal Astronomical Society*, 342(2):345–354, 2003.

Michele Cappellari. Voronoi binning: Optimal adaptive tessellations of multi-dimensional data. *arXiv preprint arXiv:0912.1303*, 2009.

J Falcón-Barroso, P Sánchez-Blázquez, A Vazdekis, E Ricciardelli, N Cardiel, AJ Cenarro, J Gorgas, and RF Peletier. An updated miles stellar library and stellar population models. *Astronomy & Astrophysics*, 532:A95, 2011.

A Beifiori, Claudia Maraston, Daniel Thomas, and J Johansson. On the spectral resolution of the miles stellar library. *Astronomy & Astrophysics*, 531:A109, 2011.

E Valenti, Manuela Zoccali, A Mucciarelli, OA Gonzalez, F Surot, Dante Minniti, M Rejkuba, L Pasquini, Giuliana Fiorentino, G Bono, et al. The central velocity dispersion

of the milky way bulge. *Astronomy & Astrophysics*, 616:A83, 2018.

James R Lewis and KC Freeman. Kinematics and chemical properties of the old disk of the galaxy. In *The World of Galaxies*, pages 202–205. Springer, 1989.